

# GEOMETRICALLY AND MATERIALLY NONLINEAR ANALYSIS FOR

## A COMPOSITE PRESSURE VESSEL

도영대, 김형근 (국방과학연구소)

### Abstract

An incremental Total Lagrangian Formulation is implemented for the finite element analysis of laminated composite pressure vessel with consideration of the material and geometric nonlinearities. For large displacements/large rotations due to geometric nonlinearities, the incremental equations are derived using a quadratic approximation for the increment of the reference vectors in terms of the nodal rotation increments. This approach leads to a complete tangent stiffness matrix. For material nonlinearity, the analysis is performed by using the piecewise linear method, taking account of the nonlinear shear stress-strain relation. The results of numerical tests include the large deflection behavior of the selected composite shell problem. When compared with the previous analysis, the results are in good agreement with them. As a practical example, filament wound pressure vessel is analyzed with consideration of the geometrically and materially nonlinearity. The numerical results agree fairly well with the existing experimental results.

### INTRODUCTION

Laminated composite structures have become increasingly popular in many engineering fields. This is due to the high specific stiffness and the high specific strength of composite structures. During the past few years, considerable efforts have been made to develop nonlinear computing programs and to predict the structural nonlinear phenomena with sufficient accuracy. These developments are justified by the need to consider extremely severe loading conditions for safety requirements, and by the important benefits resulting from weight saving in industries like aeronautics. In this paper, we first concentrate on the geometrically nonlinear analysis.

During the last decade or so, a number of finite element approaches have been proposed for the geometrically nonlinear analysis of composite shell structures [1-6]. In those papers, the element displacement field of the shell element formulation is linearized with respect to nodal rotations. This restricts the magnitude of nodal rotations during the large deformation process and necessitates very small load increments to permit good convergence. Therefore, it is necessary to develop the formulation taking the large rotations under the large load increments into consideration for the composite structures.

In the development of an element for geometrically non-linear analysis, the consideration of large rotations introduces additional difficulties due to the non-vectorial nature of finite rotations. Different formulations which show the effect of finite rotation increment on the resulting stiffness matrices have been presented by Surana [7], by Simo

and Vu Quoc [8] and by Dvorkin et al [9]. Dvorkin et al [9] used a rotation matrix developed by Argyris [10] for the finite rotation for curved beam elements. This led to the introduction of various additional geometric stiffness contributions, which were found to be necessary in order to attain the quadratic rate of convergence in Newton-Raphson iterative schemes of solutions. In this study, we extend Dvorkin's formulations in order to develop an incremental Total Lagrangian Formulation for the degenerated composite shell elements considering large displacement and large rotation. Secondly, We consider the material nonlinearity for the composite shell elements.

The stress-strain behavior of the advanced composite materials, especially graphite/epoxy, is generally classified as linear-to-failure. However, the shear stress-strain behavior of the unidirectional ply shows significant nonlinearity. Hahn and Tsai [11] suggested the cubic spline function for modeling the nonlinear inplane shear. Hu [12] showed that the nonlinear inplane shear has significant influence on the buckling and postbuckling responses of composite plates and shells, specially for those with  $[45/-45]_s$  lay up using the ABAQUS finite element program. Uemura and Fukunaga [13] showed that the nonlinear inplane shear gives significant effect on the initial failure strength for the helically filament wound cylinder composed of the graphite/epoxy. In this study, the material nonlinearity using the cubic spline function developed by Hahn and Tsai is taken into account for the incremental Total Lagrangian formulation.

the composite plate and shell examples were

solved and compared with existing alternative solutions to establish the validity of the present study. As a practical example, the filament wound pressure vessel is considered. The geometrically and materially nonlinear behavior of the filament wound chamber was studied by some authors [14-17]. Lemoine [14] analyzed the filament wound chamber composed of the kevlar/epoxy and glass/epoxy by using the axisymmetric solid element with effective modulus. He found that the analyses based on the small displacements and linear elasticity resulted in the significant discrepancies between predicted and test results. Jeusette et al [5] performed the analysis of a spherical wound satellite and the composite head of a rocket motor by using the isoparametric axisymmetrical finite elements. Uemura et al [16] performed the analysis of a rocket motor case composed of the graphite /epoxy by using the axisymmetrical shell element.

The objective of this study is to implement the large rotation theory developed by Argyris to the composite shell element with consideration of the materially nonlinearity and to analyze the filament wound pressure vessel by using the degenerated shell element with consideration of the geometrical and material nonlinearity. This degenerated shell element has the advantage of solving the problem of the composite chamber with the hole in dome such as the thrust reversal port on the motor case.

## GEOMETRIC AND KINEMATIC DESCRIPTIONS

### 2.1 Coordinate Reference Frames

Three different types of Cartesian reference frames are defined here for convenience in subsequent derivations as shown in Fig. 1.

The global coordinate system  $(x, y, z)$ , with its orthonormal base vectors  $\mathbf{e}_i$  ( $i = 1, 2, 3$ ), is used to define the element geometry and its translational displacement degrees of freedom.

The nodal coordinate system is constructed at each node, with associated unit base vectors  ${}^0\mathbf{v}_i^k$  ( $i = 1, 2, 3$ ), where  ${}^0\mathbf{v}_3^k$  coincides with the nodal fiber. During the incremental analysis, these orthogonal unit vectors are continuously updated and used as a moving basis for defining the "finite" rotational degrees of freedom at the node. This system is defined as follows:

$${}^0\mathbf{v}_3^k = \frac{{}^0\mathbf{x}_k^{top} - {}^0\mathbf{x}_k^{bot}}{\|{}^0\mathbf{x}_k^{top} - {}^0\mathbf{x}_k^{bot}\|}, \quad {}^0\mathbf{v}_1^k = \frac{\mathbf{e}_2 \times {}^0\mathbf{v}_3^k}{\|\mathbf{e}_2 \times {}^0\mathbf{v}_3^k\|} \quad (1)$$

where the vectors  ${}^0\mathbf{x}_k^{top}$  and  ${}^0\mathbf{x}_k^{bot}$  are the nodal coordinates of the top and bottom surface at node  $k$  in the initial undeformed configuration as shown in Fig. 1 where  $\mathbf{e}_2$  is the unit vector in the global  $y$ -direction. If  ${}^0\mathbf{v}_3^k$  is parallel to  $\mathbf{e}_2$ , we define  ${}^0\mathbf{v}_1^k = -\mathbf{e}_1$ . Finally, the unit vector  ${}^0\mathbf{v}_2^k$  is perpendicular to the plane defined by  ${}^0\mathbf{v}_3^k$  and  ${}^0\mathbf{v}_1^k$ .

The local lamina coordinate system  $(x', y', z')$  is a Cartesian coordinate system defined at the sampling points wherein stresses and strains are to be calculated. At any sampling point  $(\xi, \eta)$  on the lamina midsurface, an orthogonal set of local coordinate axes  $(x', y', z')$  is constructed.  $\mathbf{e}_{z'}$  is the normal unit vector and  $\mathbf{e}_{x'}$  and  $\mathbf{e}_{y'}$  are tangent to the midsurface of lamina. This system is defined as follows:

$$\mathbf{e}_{z'} = \frac{\frac{\partial \mathbf{x}}{\partial \xi} \times \frac{\partial \mathbf{x}}{\partial \eta}}{\left\| \frac{\partial \mathbf{x}}{\partial \xi} \times \frac{\partial \mathbf{x}}{\partial \eta} \right\|} \quad (2a)$$

where

$$\frac{\partial \mathbf{x}}{\partial \xi} = \left[ \frac{\partial x}{\partial \xi}, \frac{\partial y}{\partial \xi}, \frac{\partial z}{\partial \xi} \right]^T, \quad \frac{\partial \mathbf{x}}{\partial \eta} = \left[ \frac{\partial x}{\partial \eta}, \frac{\partial y}{\partial \eta}, \frac{\partial z}{\partial \eta} \right]^T \quad (2b)$$

To define the material directions in relation to the local system of axes in a consistent manner, which is a practical requirement for the analysis of anisotropic structure such as the filament wound pressure vessel, a definition of the  $\mathbf{e}_{x'}$  and  $\mathbf{e}_{y'}$  direction is adopted as three options as follows:

- right-hand -rule rotation about the normal to the shell surface, measured from the projection of the global  $i$ -axis, ( $i = x, y, z$ ) onto the shell surface as shown Fig. 2.

$$\mathbf{e}_{y'} = \frac{\mathbf{e}_{z'} \times \mathbf{e}_i}{\|\mathbf{e}_{z'} \times \mathbf{e}_i\|}, \quad \mathbf{e}_{x'} = \mathbf{e}_{y'} \times \mathbf{e}_{z'} \quad (3)$$

### 2.2 Geometry and kinematics of deformation

The global position vector to an arbitrary point in the shell element in the initial deformed configuration can be defined in terms of the natural coordinates as follows [18]:

$${}^0\mathbf{x} = \sum_{k=1}^n N_k(\xi, \eta) {}^0\bar{\mathbf{x}}_k + \sum_{k=1}^n \frac{(\zeta - \bar{\zeta}_k)}{2} a_k N_k(\xi, \eta) {}^0\mathbf{v}_3^k \quad (4a)$$

$${}^0\bar{\mathbf{x}}_k = \frac{1}{2} (1 - \bar{\zeta}_k) {}^0\mathbf{x}_k^- + \frac{1}{2} (1 + \bar{\zeta}_k) {}^0\mathbf{x}_k^+ \quad (4b)$$

where  ${}^0\bar{\mathbf{x}}_k$  is the position vector of a point O on the reference plane at nodal point k;  ${}^0\mathbf{v}_3^k$  is component of a unit fiber vector;  $\alpha_k$  is shell-thickness at nodal point k on the reference surface;  $N_k(\xi, \eta)$  are the two-dimensional shape functions associated with node k;  $n_e$  is the number of nodes per element;  ${}^0\mathbf{x}_k^-$  and  ${}^0\mathbf{x}_k^+$  are the coordinates of the top and bottom surface of the shell along each nodal fiber, respectively; a parameter  $\bar{\zeta}_k \in [-1, 1]$  which defines the location of the reference surface. The shell midsurface and the reference plane may not coincide with each other as shown in Fig. 3. Moreover, they need not be parallel with each other. This feature provides a convenient mean to model a composite shell with an internal ply delamination, a shell with stiffeners, or a skirt of the filament wound motor case.

There are five DOF per node used to parameterize the element configuration in the shell space: three global translations (u, v, w), and two "fiber" rotations  $\beta$  and  $\alpha$  about axes  $\mathbf{v}_1^k$  and  $\mathbf{v}_2^k$ . In the present incremental analysis, three successive configurations, at time "o" (initial), "t" (current) and "t + Δt" (incremented) are considered. Then, the total and incremental displacement fields of the element can be expressed as

$${}^t\mathbf{u} = \sum_{k=1}^n N_k(\xi, \eta) {}^t\bar{\mathbf{u}}_k + \sum_{k=1}^n \frac{(\bar{\zeta} - \bar{\zeta}_k)}{2} a_k N_k(\xi, \eta) ({}^t\mathbf{v}_3^k - {}^o\mathbf{v}_3^k) \quad (5a)$$

$$\Delta\mathbf{u} = \sum_{k=1}^n N_k(\xi, \eta) \Delta\bar{\mathbf{u}}_k + \sum_{k=1}^n \frac{(\bar{\zeta} - \bar{\zeta}_k)}{2} a_k N_k(\xi, \eta) ({}^{t+\Delta t}\mathbf{v}_3^k - {}^t\mathbf{v}_3^k) \quad (5b)$$

where

$${}^t\bar{\mathbf{u}}_k = {}^t\bar{\mathbf{x}}_k - {}^o\bar{\mathbf{x}}_k, \quad \Delta\bar{\mathbf{u}}_k = {}^{t+\Delta t}\bar{\mathbf{x}}_k - {}^t\bar{\mathbf{x}}_k \quad (5c)$$

Since the orthonormal system at node k rotates,

$${}^t\mathbf{v}_3^k = {}^t\mathbf{R}^k {}^o\mathbf{v}_3^k \quad (6)$$

where  ${}^t\mathbf{R}^k$  is the rotation matrix corresponding to node k at time t and is referred to the initial configuration. To go from the configuration at time "t" to the configuration at time "t + Δt", the orthogonal system at node k is only rotated. Therefore,

$${}^{t+\Delta t}\mathbf{v}_3^k = {}^{t+\Delta t}\mathbf{R}^k {}^t\mathbf{v}_3^k \quad (7a)$$

Studying this rotation, Argyris [10] arrived at

$${}^{t+\Delta t}\mathbf{R}^k = \mathbf{I}_3 + \frac{\sin \Delta\theta^k}{\Delta\theta^k} \Delta\theta^k + \frac{1}{2} \left[ \frac{\sin(\Delta\theta^k/2)}{(\Delta\theta^k/2)} \right]^2 (\Delta\theta^k)^2 \quad (7b)$$

where

$$\Delta\theta^k = \left[ \Delta\theta_1^k + \Delta\theta_2^k + \Delta\theta_3^k \right]^{1/2} \quad (7c)$$

$$\Delta\theta^k = \begin{bmatrix} 0 & -\Delta\theta_3^k & \Delta\theta_2^k \\ \Delta\theta_1^k & 0 & -\Delta\theta_1^k \\ -\Delta\theta_2^k & \Delta\theta_1^k & 0 \end{bmatrix} \quad (7d)$$

Note that the  $\Delta\theta_i^k$  are not independent rotations around the global axes but are the components of the matrix defined in Eq. (7d), which characterized a rotation around the rotation axis.

In a very elegant way, Argyris proved that Eq. (7b) can be rewritten as

$${}^{t+\Delta t}\mathbf{R}^k = \mathbf{I}_3 + \Delta\theta^k + \frac{1}{2!} (\Delta\theta^k)^2 + \frac{1}{3!} (\Delta\theta^k)^3 + \dots \quad (8)$$

Because the incremental rotations are finite, we keep the linear and the quadratic terms in Eq. (8). Substituting Eq. (8) into Eq. (7a), we can write the following

$${}^{t+\Delta t}\mathbf{v}_3^k - {}^t\mathbf{v}_3^k = \Delta\theta^k {}^t\mathbf{v}_3^k + \frac{1}{2} \Delta\theta^k \Delta\theta^k {}^t\mathbf{v}_3^k \quad (9a)$$

Eq. (9a) can be rewritten as vector forms.

$${}^{t+\Delta t}\mathbf{v}_3^k - {}^t\mathbf{v}_3^k = \Delta\theta^k \times {}^t\mathbf{v}_3^k + \frac{1}{2} \Delta\theta^k \times \Delta\theta^k \times {}^t\mathbf{v}_3^k \quad (9b)$$

Since the incremental rotations  $\Delta\alpha_k$  and  $\Delta\beta_k$  in the shell element are given with respect to the nodal coordinate frame  ${}^t\mathbf{v}_1^k - {}^t\mathbf{v}_2^k - {}^t\mathbf{v}_3^k$  as shown in Fig. 1, the vector crossproduct in Eq. (9b) can be effectively evaluated in nodal coordinate frame. In this case, the vector  $\Delta\theta^k$  is defined as follows:

$$\Delta\theta^k = \Delta\beta_k {}^t\mathbf{v}_1^k + \Delta\alpha_k {}^t\mathbf{v}_2^k \quad (10)$$

Substituting Eq. (10) into Eq. (9b), we can obtain

$${}^{t+\Delta t}\mathbf{v}_3^k - {}^t\mathbf{v}_3^k = \Delta\alpha {}^t\mathbf{v}_1^k - \Delta\beta {}^t\mathbf{v}_2^k - \frac{1}{2} (\Delta\alpha^2 + \Delta\beta^2) {}^t\mathbf{v}_3^k \quad (11)$$

Substituting Eq. (11) into Eq. (5b), we can obtain

$$\Delta\mathbf{u} = \Delta\mathbf{u}_L + \Delta\mathbf{u}_R \quad (12a)$$

$$\Delta\mathbf{u}_L = \sum_k N_k \Delta\bar{\mathbf{u}}_k + \sum_k \frac{(\bar{\zeta} - \bar{\zeta}_k)}{2} a_k N_k [\Delta\alpha_k {}^t\mathbf{v}_1^k - \Delta\beta_k {}^t\mathbf{v}_2^k] \quad (12b)$$

$$\Delta\mathbf{u}_R = \sum_k \frac{(\bar{\zeta} - \bar{\zeta}_k)}{2} a_k N_k \left( -\frac{1}{2} (\Delta\alpha_k^2 + \Delta\beta_k^2) {}^t\mathbf{v}_3^k \right) \quad (12c)$$

where  $\Delta \mathbf{u}_L$  is term obtained from considering only the infinitesimal rotation increment and  $\Delta \mathbf{u}_R$  is the extra term from considering the finite rotation increment.

The updated vectors  ${}^{t+\Delta t} \mathbf{v}_i^k - {}^{t+\Delta} \mathbf{v}_2^k - {}^{t+\Delta} \mathbf{v}_3^k$  of nodal coordinate system are obtained as follows:

$${}^{t+\Delta} \mathbf{v}_i^k = \mathbf{v}_i^k + \mathbf{g} \Delta \theta \times \mathbf{v}_i^k + \mathbf{g} \Delta \theta \times \Delta \theta \times \mathbf{v}_i^k \quad (i=1,2,3) \quad (13a)$$

where

$$\mathbf{g}_2 = \frac{\sin \Delta \theta^k}{\Delta \theta^k}, \quad \mathbf{g}_1 = \frac{1}{2} \left[ \frac{\sin(\Delta \theta^k / 2)}{(\Delta \theta^k / 2)} \right]^2, \quad (13b)$$

$$\Delta \theta^k = (\Delta \beta_k^2 + \Delta \alpha_k^2)^{1/2}$$

Substituting Eq. (10) into Eq. (13a), we obtain the updated nodal vectors at time "t + Δt" as follows:

$$\begin{Bmatrix} {}^{t+\Delta} \mathbf{v}_1^k \\ {}^{t+\Delta} \mathbf{v}_2^k \\ {}^{t+\Delta} \mathbf{v}_3^k \end{Bmatrix} = \begin{bmatrix} 1 - \mathbf{g}_2 \Delta \alpha_k^2 & \mathbf{g}_2 \Delta \alpha_k \Delta \beta_k & -\mathbf{g}_2 \Delta \alpha_k \\ \mathbf{g}_2 \Delta \alpha_k \Delta \beta_k & 1 - \mathbf{g}_2 \Delta \beta_k^2 & \mathbf{g}_2 \Delta \beta_k \\ \mathbf{g}_2 \Delta \alpha_k & -\mathbf{g}_2 \Delta \beta_k & 1 - \mathbf{g}_2 (\Delta \alpha_k^2 + \Delta \beta_k^2) \end{bmatrix} \begin{Bmatrix} \mathbf{v}_1^k \\ \mathbf{v}_2^k \\ \mathbf{v}_3^k \end{Bmatrix} \quad (14)$$

## FORMULATION OF THE INCREMENTAL EQUATIONS OF EQUILIBRIUM

In the geometrically nonlinear analysis Total Lagrangian (T.L.) formulation has been considered. In the T.L. formulation, all current static and kinematic variables are referred to the initial configuration before the deformation (say at time "0"). T.L. formulation includes all kinematic nonlinear effects due to large displacement and rotations. For the formulation, the local Cartesian coordinate system is used.

### 3.1 Total Lagrangian Formulation (T.L.)

In the Total Lagrangian formulation at time  $t + \Delta t$ , all variables are referred to the initial configuration at time "0" and the governing equation with incremental terms is

$$\int_{\Omega_V} \Delta S_{ij} \delta \Delta E_{ij}^0 dV + \int_{\Omega_V} {}^t S_{ij} \delta \Delta \eta_{ij}^0 dV = {}^{t+\Delta t} \delta W - \int_{\Omega_V} {}^t S_{ij} \delta \Delta e_{ij}^0 dV \quad (15)$$

where  ${}^{t+\Delta t} \delta W$  is the external incremental virtual work at the current load increment;  $\Delta E_{ij}$  is the incremental Green-Lagrange strain tensor which can be divided into two parts so that

$$\Delta E_{ij} = \Delta e_{ij} + \Delta \eta_{ij} \quad (16a)$$

where

$$\Delta e_{ij} = \frac{1}{2} (\Delta_0 u_{i,j} + \Delta_0 u_{j,i} + {}^t_0 u_{k,j} \Delta_0 u_{k,i} + {}^t_0 u_{k,i} \Delta_0 u_{k,j}) \quad (16b)$$

$$\Delta \eta_{ij} = \frac{1}{2} (\Delta_0 u_{k,i} \Delta_0 u_{k,j}) \quad (16c)$$

and  ${}^t S_{ij}$  is the second Piola-Kirchhoff stresses and subscript 0 and superscript t given in front of the stress symbols denote that the stresses at time t are referred to the configuration at time 0. Incremental second Piola-Kirchhoff stresses  $\Delta S_{ij}$  can be expressed as

$$\Delta S_{ij} = {}^0 C_{ijkl} \Delta E_{ij} \approx {}^0 C_{ijkl} \Delta e_{ij} \quad (17)$$

A matrix formulation of the incremental equilibrium equation (15) is obtained by considering each integral in Eq. (15) separately. Accordingly,

$$\int_{\Omega_V} \{ \delta \Delta e \}^T [ {}^0 C ] \{ \Delta e \}^0 dV + \int_{\Omega_V} \{ \delta \Delta \eta \}^T [ {}^0 S ] \{ \Delta \eta \}^0 dV = {}^{t+\Delta t} \delta W - \int_{\Omega_V} \{ \delta \Delta e \}^T [ {}^0 S ]^0 dV \quad (18a)$$

where  $[ {}^0 C ]$  is the stiffness matrix of the lamina properties, which is defined as Eq. (30a).

$$\{ {}^0 S \} = [ {}^0 S_{xx}, {}^0 S_{yy}, {}^0 S_{xy}, {}^0 S_{xz}, {}^0 S_{yz} ]^T \quad (18b)$$

$$\{ \Delta e \} = [ \Delta e_{xx}, \Delta e_{yy}, 2\Delta e_{xy}, 2\Delta e_{xz}, 2\Delta e_{yz} ]^T \quad (18c)$$

$$[ {}^0 S ] = \begin{bmatrix} S_{11} \mathbf{I} & S_{12} \mathbf{I} & S_{13} \mathbf{I} \\ S_{12} \mathbf{I} & S_{22} \mathbf{I} & S_{23} \mathbf{I} \\ S_{13} \mathbf{I} & S_{23} \mathbf{I} & \mathbf{0} \end{bmatrix} \quad (18d)$$

and  $\mathbf{I}$  is the third order identity matrix and  $\mathbf{0}$  is the third order zero matrix. Finally,  $\Delta \hat{\mathbf{u}}^T$  is a vector of Cartesian derivatives defined by

$$\{ \Delta \hat{\mathbf{u}} \} = [ \Delta u_x, \Delta v_x, \Delta w_x, \Delta u_y, \Delta v_y, \Delta w_y, \Delta u_z, \Delta v_z, \Delta w_z ]^T \quad (19)$$

### 3.2 strain-displacement relationship

The incremental displacement derivatives with respect to isoparametric coordinate can be obtained from Eq. (12a) and given by

$$\begin{Bmatrix} \partial \Delta u / \partial \xi \\ \partial \Delta u / \partial \eta \\ \partial \Delta u / \partial \xi_L \end{Bmatrix} = \sum_{k=1}^n \begin{bmatrix} N_{kx} & N_{ky} & N_{kz} & -N_{kx} & -N_{ky} & -N_{kz} \\ N_{kx} & N_{ky} & N_{kz} & -N_{kx} & -N_{ky} & -N_{kz} \\ 0 & N_{kx} & -N_{ky} & 0 & 0 & 0 \end{bmatrix} \begin{Bmatrix} \Delta \hat{\mathbf{u}} \\ \Delta \alpha_k \end{Bmatrix} \quad (20a)$$

$$\begin{Bmatrix} \partial \Delta u / \partial \xi \\ \partial \Delta u / \partial \eta \\ \partial \Delta u / \partial \xi_R \end{Bmatrix} = \sum_{k=1}^n \begin{bmatrix} 0 & -N_{kx} & -N_{ky} & -N_{kx} & -N_{ky} \\ 0 & -N_{kx} & -N_{ky} & -N_{kx} & -N_{ky} \\ 0 & -N_{kx} & -N_{ky} & -N_{kx} & -N_{ky} \end{bmatrix} \begin{Bmatrix} \Delta \hat{\mathbf{u}} \\ \Delta \alpha_k \end{Bmatrix} \quad (20b)$$

where

$$\mathbf{g}_{1i}^k = \frac{1}{2} \mathbf{a}_k^t \mathbf{v}_{1i}^k, \mathbf{g}_{2i}^k = \frac{1}{2} \mathbf{a}_k^t \mathbf{v}_{2i}^k, \mathbf{g}_{3i}^k = \frac{1}{2} \mathbf{a}_k^t \mathbf{v}_{3i}^k \quad (20c)$$

and  $\Delta u_i$  is the component of the incremental displacement such as  $(\Delta u \ \Delta v \ \Delta w)$  of a generic point on the shell element;  $({}^t \mathbf{v}_{1i}^k, {}^t \mathbf{v}_{2i}^k, {}^t \mathbf{v}_{3i}^k)$  is the component of the unit vectors  $({}^t \mathbf{v}_1^k, {}^t \mathbf{v}_2^k, {}^t \mathbf{v}_3^k)$  in the direction  $i$  and at nodal point  $k$ .

The displacement derivatives at time  $t$  with respect to isoparametric coordinates can be given by

$$\begin{Bmatrix} \partial^t u_i / \partial \xi \\ \partial^t u_i / \partial \eta \\ \partial^t u_i / \partial \zeta \end{Bmatrix} = \sum_{k=1}^n \begin{Bmatrix} N_{k,\xi} & N_{k,\xi} \frac{\mathbf{a}_k(\zeta - \bar{\zeta}_k)}{2} \\ N_{k,\eta} & N_{k,\eta} \frac{\mathbf{a}_k(\zeta - \bar{\zeta}_k)}{2} \\ 0 & N_k \frac{\mathbf{a}_k}{2} \end{Bmatrix} \begin{Bmatrix} \bar{\mathbf{u}}_i^k \\ {}^t \mathbf{v}_{1i}^k - {}^t \mathbf{v}_{3i}^k \end{Bmatrix} \quad (21)$$

To evaluate the local strain components, the derivatives of  $u', v', w'$  with respect to  $x', y', z'$  are obtained from the transformation as follows:

$$\frac{\partial(u, v, w)}{\partial(x, y, z)} = [\mathbf{e}_x, \mathbf{e}_y, \mathbf{e}_z]^T \left[ \frac{\partial(x, y, z)}{\partial(\xi, \eta, \zeta)} \right]^{-1} \frac{\partial(u, v, w)}{\partial(x, y, z)} [\mathbf{e}_x, \mathbf{e}_y, \mathbf{e}_z] \quad (22)$$

The linear incremental strain vectors in the local coordinate system may be expressed as

$$\{\Delta \mathbf{e}'\} = \mathbf{H} \{\Delta \hat{\mathbf{u}}'\} + \mathbf{A} \{\Delta \hat{\mathbf{u}}'\} \quad (23a)$$

where  $\Delta \hat{\mathbf{u}}' \mathbf{t}$  is a vector of local Cartesian derivatives defined by Eq. (19), and matrices  $\mathbf{H}$  and  $\mathbf{A}$  are defined as

$$\mathbf{H} = \begin{bmatrix} 1 & 0 & 0 & 0 & 0 & 0 & 0 & 0 & 0 \\ 0 & 0 & 0 & 0 & 1 & 0 & 0 & 0 & 0 \\ 0 & 1 & 0 & 1 & 0 & 0 & 0 & 0 & 0 \\ 0 & 0 & 1 & 0 & 0 & 0 & 1 & 0 & 0 \\ 0 & 0 & 0 & 0 & 0 & 1 & 0 & 1 & 0 \end{bmatrix} \quad (23b)$$

$$\mathbf{A} = \begin{bmatrix} {}^t \mathbf{u}'_{,x'} & 0 & 0 \\ 0 & {}^t \mathbf{u}'_{,y'} & 0 \\ {}^t \mathbf{u}'_{,y'} & {}^t \mathbf{u}'_{,x'} & 0 \\ {}^t \mathbf{u}'_{,z'} & 0 & {}^t \mathbf{u}'_{,x'} \\ 0 & {}^t \mathbf{u}'_{,z'} & {}^t \mathbf{u}'_{,y'} \end{bmatrix} \quad (23c)$$

$${}^t \mathbf{u}'_{,i'} = \left[ {}^t u'_{,i'}, {}^t v'_{,i'}, {}^t w'_{,i'} \right]^T \quad (i' = x', y', z') \quad (23d)$$

The vector of local Cartesian derivatives  $\{\Delta \hat{\mathbf{u}}'\}$  is related to the incremental nodal displacement vector using Eq. (20) and (22).

$$\{\Delta \hat{\mathbf{u}}'\} = \mathbf{G} \{\Delta \mathbf{U}\} \quad (24a)$$

where  $\{\Delta \mathbf{U}\}$  is incremental nodal displacement vector defined by

$$\{\Delta \mathbf{U}\} = [\Delta \bar{\mathbf{u}}, \Delta \bar{\mathbf{v}}, \Delta \bar{\mathbf{w}}, \Delta \alpha_1, \Delta \beta_1, \dots, \Delta \alpha_p, \Delta \beta_p, \Delta \alpha_p, \Delta \beta_p]^T \quad (24b)$$

and matrix  $\mathbf{G}$  separates into

$$\mathbf{G} = \mathbf{G}_L + \mathbf{G}_R(\Delta \alpha, \Delta \beta) \quad (24c)$$

where  $\mathbf{G}_L$  is matrix obtained from considering only the infinitesimal rotation increment and  $\mathbf{G}_R(\Delta \alpha, \Delta \beta)$  is the extra matrix from considering the finite rotation increment and the function of  $\Delta \alpha, \Delta \beta$ . Using Eq. (23a) and (24a), we can write the linear incremental strain vectors as follows.

$$\{\Delta \mathbf{e}'\} = \left[ (\mathbf{B}_L + \mathbf{B}_R(\Delta \alpha, \Delta \beta)) + \mathbf{A}(\mathbf{G}_L + \mathbf{G}_R(\Delta \alpha, \Delta \beta)) \right] \{\Delta \mathbf{U}\} \quad (25a)$$

where

$$\mathbf{B}_L = \mathbf{H} \mathbf{G}_L, \quad \mathbf{B}_R(\Delta \alpha, \Delta \beta) = \mathbf{H} \mathbf{G}_R(\Delta \alpha, \Delta \beta) \quad (25b)$$

Substituting Eq. (24a), (25a) into Eq.(18a) and retaining the linear terms only, we obtain the following incremental equilibrium equation

$$(\mathbf{K} + \mathbf{K}_\sigma + \mathbf{K}_R) \{\Delta \mathbf{U}\} = \{\mathbf{F}\} - \int_{,v} \left[ \mathbf{B}_L + \mathbf{A} \mathbf{G}_L \right]^T \left[ {}^t \mathbf{S}' \right] {}^0 dV \quad (26a)$$

in which

$$\mathbf{K} = \int_{,v} \left[ \mathbf{B}_L + \mathbf{A} \mathbf{G}_L \right]^T \left[ {}^t \mathbf{C}' \right] \left[ \mathbf{B}_L + \mathbf{A} \mathbf{G}_L \right] {}^0 dV \quad (26b)$$

$$\mathbf{K}_\sigma = \int_{,v} \mathbf{G}_L^T \left[ {}^t \mathbf{S}' \right] \mathbf{G}_L {}^0 dV \quad (26c)$$

$$\mathbf{K}_R \{\Delta \mathbf{U}\} = \int_{,v} \left[ \mathbf{B}_R + \mathbf{A} \mathbf{G}_R \right]^T \left[ {}^t \mathbf{S}' \right] {}^0 dV \quad (26d)$$

where  $\mathbf{K}_R$  is the diagonal matrix occurred due to the effects of the nonlinear functions of rotations. The diagonal terms in matrix  $\mathbf{K}_R$  have zero values for the terms corresponding to the displacement degrees of freedom, and they have value for the terms corresponding to the rotational degrees of freedom.

### 3.3 Constitutive modeling of lamina.

To model the nonlinear in-plane shear behavior as shown in Fig. 4, the nonlinear strain-stress relation for a composite suggested by Hahn and Tsai [11] is adopted in this study, which is given as follows:

$$E_{LT} = \left( \frac{1}{G_{LT}} \right) S_{LT} + \alpha S_{LT}^3 \quad (27)$$

where subscript L and T are coordinates parallel and normal to the fibers of material coordinate system;  $E_{LT}$  and  $S_{LT}$  denote the shear component of the Green-Lagrange strains and the second Piola-Kirchhoff stresses, respectively;  $G_{LT}$  is the initial shear modulus and  $\alpha$  is the nonlinear parameter of the material that has to be determined experimentally. By taking the partial derivative of Eq. (27) with respect to  $E_{LT}$ , the tangent shear modulus can be obtained as follows:

$$\bar{G}_{LT} = \frac{\partial S_{LT}}{\partial E_{LT}} = \frac{1}{\frac{1}{G_{LT}} + 3\alpha S_{LT}^2} \quad (28a)$$

$$\bar{G}_{L\zeta} = \frac{\partial S_{L\zeta}}{\partial E_{L\zeta}} = \frac{1}{\frac{1}{G_{L\zeta}} + 3\alpha S_{L\zeta}^2} \quad (28b)$$

where  $\bar{G}_{LT}$  is the tangent shear modulus in the (L-T) plane of material axis and  $\bar{G}_{L\zeta}$  is the tangent shear modulus in the (L- $\zeta$ ) plane in which  $\zeta$  is the normal axis to the (L-T) plane. Since the stress analysis is performed by the incremental load method, the incremental constitutive equations referred to the material coordinate system of unidirectional lamina within the time step "t"  $\rightarrow$  "t +  $\Delta t$ " can be expressed by

$$\begin{Bmatrix} \Delta S_{L\zeta} \\ \Delta S_{LT} \\ \Delta S_{L\zeta} \\ \Delta S_{L\zeta} \\ \Delta S_{L\zeta} \end{Bmatrix}_m = \begin{bmatrix} \frac{E_{L\zeta}}{1-\nu_{L\zeta}\nu_{L\zeta}} & \frac{E_{LT}\nu_{LT}}{1-\nu_{LT}\nu_{LT}} & 0 & 0 & 0 \\ \frac{E_{LT}\nu_{LT}}{1-\nu_{LT}\nu_{LT}} & \frac{E_{LT}}{1-\nu_{LT}\nu_{LT}} & 0 & 0 & 0 \\ 0 & 0 & \bar{G}_{LT} & 0 & 0 \\ 0 & 0 & 0 & k\bar{G}_{L\zeta} & 0 \\ 0 & 0 & 0 & 0 & k\bar{G}_{L\zeta} \end{bmatrix} \begin{Bmatrix} \Delta e_{L\zeta} \\ \Delta e_{LT} \\ 2\Delta e_{L\zeta} \\ 2\Delta e_{L\zeta} \\ 2\Delta e_{L\zeta} \end{Bmatrix}_m \quad (29)$$

where subscript m denotes the m-th particular lamina and  $(k = \frac{2}{3})$  denote shear correction factor. The components of matrix are considered to be constant before initial failure and  $\bar{G}_{LT}$  and  $\bar{G}_{L\zeta}$  are assumed as constant in a piece-wise increment.

For the evaluation of element stiffness, the material matrix referring to material coordinates must be transformed to the local coordinates system. By transformation, we can obtain the incremental

stress-strain relations as follows:

$$\{\Delta S'\} = [{}^0C']\{\Delta e'\}, [{}^0C'] = T^T {}^0Q T \quad (30a)$$

where  ${}^0Q$  is the stiffness matrix defined in Eq. (29), and

$$T = \begin{bmatrix} m^2 & n^2 & mn & 0 & 0 \\ n^2 & m^2 & -mn & 0 & 0 \\ -2mn & 2mn & m^2 - n^2 & 0 & 0 \\ 0 & 0 & 0 & m & n \\ 0 & 0 & 0 & -n & m \end{bmatrix} \quad (30b)$$

$$m = \cos\theta, n = \sin\theta$$

where  $\theta$  is the fiber angle between the material coordinate system and local coordinate system.

Since element geometry and fiber directions are independent of each other, the fiber angle  $\theta$  is not constant within the element for the case of the filament wound chamber. Therefore, by specifying the  $\theta$ -angle at each nodal point of the element and using the 2-D shape function  $N(\xi, \eta)$ , one can interpolate the  $\theta$ -angle at the Gaussian point.

### 3.4 Layered Model

The integral indicated in  $K$ ,  $K_\sigma$ , and  $K_R$  of Eq. (26a) is evaluated numerically by Gauss Quadrature formula. However, the elasticity matrix is different from layer to layer and not a continuous function of  $\zeta$ . The integration is carried out by splitting the limits through each layer. In order to apply the known coefficients of the Gaussian quadrature, the limits of integration should be from -1 to 1. This is achieved by using a layered approach [19], wherein a mid-point rule integration scheme is adopted for each layer. Layers of different thickness can be employed, as well as different number of layers per element. The specification of the layer thickness in terms of the curvilinear coordinate,  $\zeta$ , permits the variation of the layer thickness as the shell thickness varies. The integration by using the layered approach can be written as

$$\int_{V_k} R(x,y,z) d^3V = \int_{-1}^1 \int_{-1}^1 \sum_{k=1}^N F(\xi, \eta, \zeta_k) J(\xi, \eta, \zeta_k) \Delta \zeta_k d\xi d\eta \quad (31a)$$

$$\Delta \zeta_k = \frac{2 h_k}{h}, \zeta_k = -1 + \sum_{j=1}^{k-1} \Delta \zeta_j + \frac{\Delta \zeta_k}{2} \quad (31b)$$

where  $h$  is the total thickness of laminate in a element;  $h_k$  is k-th layer thickness of laminate;  $N$  is the total number of laminate in a element.

## SOLUTION PROCEDURES

Once assembled, the linearized equations above are utilized in the following incremental - iterative full Newton-Raphson scheme [20] for the solution of the incremental nodal displacements in the  $i$ -th iteration within the time step " $t$ "  $\rightarrow$  " $t + \Delta t$ ".

$$({}^{t+\Delta} \mathbf{K} + {}^{t+\Delta} \mathbf{K}_\sigma + {}^{t+\Delta} \mathbf{K}_R)^{(i-1)} \Delta \mathbf{U}^{(i)} = {}^{t+\Delta} \mathbf{P} - {}^{t+\Delta} \mathbf{F}^{(i-1)} \quad (32)$$

The displacement increment is used to next displacement and nodal vector as follows:

$$\mathbf{U}^{(i)} = \mathbf{U}^{(i-1)} + \Delta \mathbf{U}^{(i)} \quad (33)$$

$$\begin{Bmatrix} {}^{t+\Delta} \mathbf{v}_1^k \\ {}^{t+\Delta} \mathbf{v}_2^k \\ {}^{t+\Delta} \mathbf{v}_3^k \end{Bmatrix}^{(i)} = \begin{bmatrix} 1 - g_1 \Delta \alpha_k^2 & g_1 \Delta \alpha_k \Delta \beta_k & -g_2 \Delta \alpha_k \\ g_2 \Delta \alpha_k \Delta \beta_k & 1 - g_2 \Delta \beta_k^2 & g_1 \Delta \beta_k \\ g_2 \Delta \alpha_k & -g_2 \Delta \beta_k & 1 - g_2 (\Delta \alpha_k^2 + \Delta \beta_k^2) \end{bmatrix}^{(i)} \begin{Bmatrix} {}^{t+\Delta} \mathbf{v}_1^k \\ {}^{t+\Delta} \mathbf{v}_2^k \\ {}^{t+\Delta} \mathbf{v}_3^k \end{Bmatrix}^{(i-1)} \quad (34)$$

Using Eq. (34), the incremental displacement derivatives of Eq. (20a) and Eq.(20b) and the displacement derivatives of Eq.(21) are updated and from that incremental displacement derivatives and that displacement derivatives, the matrices of  $\mathbf{B}, \mathbf{A}, \mathbf{G}$  and the increment strains of  $\Delta \mathbf{e}$  are updated. Finally, the stress is updated as follows:

$${}^{t+\Delta} \mathbf{S}^{(i)} = {}^{t+\Delta} \mathbf{S}^{(i-1)} + \mathbf{C}({}^{t+\Delta} \mathbf{S}^{(0)}) \Delta \mathbf{e}^{(i)} \quad (35)$$

## NUMERICAL TESTS

### 5.1. Geometrically nonlinear analysis involving large rotations

Numerical tests were conducted to check the ability of the present formulation to allow large displacements and large rotations.

#### 5.1.1. A cantilever beam under tip roll-up moment

Eight elements are used to idealize a cantilever subjected to an end moment as shown in Fig. 5. This problem is chosen to examine a geometrically nonlinear problem with large displacements and rotations.

An initially straight beam is under tip roll-up moment. The tip moment is applied until the beam is rolled up to form a circle to obtain a  $360^\circ$  rolled-up configuration. The beam is 12 in. long, while thickness and width are both 1 in. The material properties used are Young's Modulus  $E = 30 \times 10^6$  psi and  $\nu = 0.0$ . In Fig. 5, it is shown that the exact  $360^\circ$  rolled-up configurations are obtained when the tip moments approaches the value of  $2\pi EI / L$  which is divided into 10 load increments, where  $EI$  is the bending stiffness of the

beam. Each rolled-up shape is achieved with only one load step. The present results agree well with those reported in Surana [7].

#### 5.1.3. Composite cylindrical shell under uniformly distributed load.

Fig. 6 shows a  $[0/90^\circ]$  composite cylindrical shell under uniformly distributed load. All boundaries are clamped and the dimensions are  $R = 2540$  in.,  $L = 508$  in.,  $t = 2.54$  in. and  $\theta = 0.2$  rad.

Elastic properties are as follows:

$$E_{LL} = 25 \times 10^6 \text{ psi}, E_{TT} = 10^6 \text{ psi},$$

$$G_{LT} = G_{Lz} = 0.5 \times 10^6 \text{ psi}, G_{Tz} = 0.2 \times 10^6 \text{ psi}, \nu_{LT} = 0.25.$$

Because of the symmetry of the structure, only a quarter of the cylindrical shell was modeled with  $3 \times 3$  elements. Fig. 7 shows the vertical deflections at the center of the shell under increasing uniform pressure up to  $P = 2.0$  psi.

In here, Two load increment methods are compared. Firstly, The load increment has 1 increment with 0.4 time-end, 10 equal increments with 0.6 time-end, 20 equal increments with 0.8 time-end, and 10 equal increments with 1.0 time-end. Secondly, the load increment has 1 increment with 0.4 time-end and 10 equal increments with 1.0 time-end. The results of the two methods show the exactly same values and good convergence characteristics. The present results agree well with those reported in Kim et al [6].

### 5.2. Materially nonlinear analysis of the helical-wound cylinder

For the materially nonlinear analysis, we perform an analysis of the graphite fiber helical-wound cylinders under internal pressure. In this analysis the helical-wound cylinder is assumed to an angle-ply laminate consisting of  $\pm \theta$  laminate. In order to check the validity of the numerical approach mentioned above, the filament wound cylinder in Fig. 8 is adopted, for it was studied by Uemura et al [13]. They studied it by the analytic method and carried out the hydraulic pressure test by use of a handy pump. The dimensions of the cylinder are  $L = 550$  mm in length,  $D = 100$  mm in inner diameter, and  $h = 2$  mm in thickness. Each cylinders are consisted of  $[\pm \theta]_{8T}$ . Elastic properties are as follows:

$$E_{LL} = 12.5 \times 10^{10} \text{ Pa}, E_{TT} = 0.854 \times 10^{10} \text{ Pa},$$

$$G_{LT} = G_{Lz} = G_{Tz} = 0.511 \times 10^{10} \text{ Pa}, \nu_{LT} = 0.27,$$

$$\alpha = 52.77 \times 10^{-27} (\text{Pa})^{-3}$$

where  $\alpha$  is the nonlinear parameter. Because of the

symmetry of the structure, only a half of the cylinder was modeled with 6 elements in the hoop direction and 23 elements in the longitudinal direction. Internal pressure is applied and the equivalent nodal forces of the pressure applied to the cap of the cylinder are applied as shown in Fig. 8. The symmetry boundary condition is applied along the edge of longitudinal axis; the clamped boundary condition except displacement  $-u$  is applied at the reinforced parts; The displacement  $-u$  is fixed at the central line of the cylinder. Two kinds of laminates such as  $[\pm 35^\circ]_{ST}$ ,  $[\pm 45^\circ]_{ST}$  are considered in order to analyze the effect of the winding angle on the structure.

As the results of the analysis, the average stress such as  $\bar{\sigma} = pr/4h$  versus the strain curves at the center of the cylinder are plotted. The nonlinearity in shear behavior is found in Fig.9. to give large strains, especially in the range of  $30^\circ < \theta < 55^\circ$ . Therefore, It is evident that the nonlinearity should be taken into consideration when high shear stress exists. The present results agree very well with those reported in Uemura et al [13].

### 5.3 The geometrically nonlinear and the materially nonlinear analysis of the filament wound pressure chamber

The objective of this part is to show that the analytical method to predict the deflections of the filament wound chambers must account for the geometric and material non-linearity. Filament wound chambers have the dome contours in which the composite thickness and the winding angle varied along the meridional line of the dome. The dome parts is composed of the angle ply laminate which is assumed to show the materially nonlinear behavior, so it is necessary to analyze the chamber with consideration of the material nonlinearity.

For filament wound chambers, the two kinds of winding method can be considered such as the geodesic winding method and the polar winding method. The geodesic winding method is used to produce the chamber with equal polar openings so that the dome shape of the forward and after parts are same. In the geodesic dome, the stress of the filament is constant. The polar winding method is used to produce the chamber with unequal polar opening so that the forward and after dome shape is different each other. In this study, We consider only the filament wound chamber with the geodesic dome. We briefly explain the design method of the geodesic dome shape. The detailed design method can be found in Reference[16].

The dome shape of the geodesic can be described as follows:

$$\zeta = \frac{1}{2} \int_{\rho}^1 \left\{ \rho^2 / \sqrt{(1-\rho^2)(\rho^2-\rho_1^2)(\rho^2-\rho_2^2)} \right\} d(\rho^2) \quad (36)$$

$$= [\rho_2^2 F(\psi, k) + (1-\rho_2^2) E(\psi, k)] / \sqrt{1-\rho_2^2}$$

where

$\rho = r/r_0$ ,  $\rho_0 = r_1/r_0$ , and  $\zeta = z/r_0$  are the normalized dimensions;  $r_0$  is the radius of the cylinder;  $r_1$  is the radius of the opening of the dome;  $r$  is the local radius of the dome;  $z$  is the height from the bottom of dome;  $F(\psi, k)$  and  $E(\psi, k)$  are the first and second kind of elliptic integral, respectively. And  $\psi, k$  are described as follows:

$$\sin^2 \psi = (1-\rho^2)/(1-\rho_1^2), \quad k = (1-\rho_1^2)/(1-\rho_2^2) \quad (37)$$

where

$$\rho_1^2 = \frac{1}{2} \left\{ \sqrt{(1+3\rho_0^2)/(1-\rho_0^2)} - 1 \right\},$$

$$\rho_2^2 = -\frac{1}{2} \left\{ \sqrt{(1+3\rho_0^2)/(1-\rho_0^2)} + 1 \right\}$$

Finally, the winding angle with respect to the meridional line and the thickness of the arbitrary point of the dome can be described as

$$\sin \omega = r_1/r \quad (38a)$$

$$h = h_0 r_0 \cos \omega_0 / r \cos \omega \quad (38b)$$

where  $h_0$  and  $\omega_0$  are the thickness and the winding angle of the bottom of the dome, respectively.

The isotensoid CFRP pressure vessel which was used for the kick-motor-case to launch the scientific satellite "zikiken" in Japan is selected for the model. The geometry of that chamber is shown in Fig. 10. The dome shapes, the angle variation, and the thickness variation along the composite dome is shown in Fig. 11. The composite chamber is composed of 3-angle layer such as  $[\pm \theta]_{ST}$  for the dome part; the thickness of bottom of the dome is the 2.3 mm; The cylinder part is reinforced with 6-hoop plies of the 2.4 mm so that the sequence is  $[\pm \theta]_{ST} / [90]_{ST}$  from the inner layer to outer layer, from the junction line of the dome and cylinder to 50.5mm along the meridional line, hoop-ply is reinforced as shown in Fig. 11. Elastic properties are as follows:

$$E_{LT} = 12.5 \times 10^{10} \text{ Pa}, \quad E_{TT} = 0.854 \times 10^{10} \text{ Pa},$$

$$G_{LT} = G_{L\zeta} = G_{T\zeta} = 0.511 \times 10^{10} \text{ Pa}, \quad \nu_{LT} = 0.27,$$

$$\alpha = 52.77 \times 10^{-27} (\text{Pa})^{-3}.$$

Because of the symmetry of the structure, only a



quarter of the cylinder is modeled with 10 elements in the hoop direction and 24 elements in the longitudinal direction. The symmetry boundary conditions are applied along the edge lines of the cylinder but at the polar boss parts, all displacements and rotations are fixed except the axial displacement.

The composite chamber is subjected to internal pressure up to  $P = 5.39 \text{ MPa}$  which has 20 equal load increments, but the equivalent axial nodal forces of the pressure is applied at the polar boss parts.

In Fig. 12, the initial structure and the deformed shapes for the linear case and the nonlinear case are presented at pressure  $P = 5.39 \text{ MPa}$ . In Fig. 14 for the linear and nonlinear case at pressure  $P = 4.31 \text{ MPa}$ , the strain variations of the entire model are shown in the hoop and meridional directions, respectively. The abscissa of the graphs is the distance from the junction of cylinder and dome. These plots show the difference in the predicted dome deflections between the linear and non-linear analyses. This deflected shape from linear analysis as shown in Fig. 12b exhibits significant flexure effects at the dome-cylinder junction area and at the tip of the polar boss, because of the sudden increase in the chamber stiffness in these areas. These changes in flexural stiffness are due to the presence of hoop windings in the cylinder and of the polar boss at the other end. Since pressure is assumed to be applied on the undeformed shape in the linear analysis, flexure effects become proportional to pressure and thus remain significant compared with membrane effects at any pressure level. The nonlinear analysis leads to almost uniform, smoothly-varying deflections of the dome as shown in Fig 12c, exhibiting a radial growth at any location. This type of analysis, accounting for the changes of the dome curvature during the pressurization, results in quite negligible flexure effects compared to membrane effects at high pressure levels due to the internal pressure applied to the deformed shape.

Looking into the strain variations as shown in Fig. 13 for the nonlinear analysis, the meridional strains are uniform at the dome but the meridional strains increase due to the increment of winding angle and flexure effects near the tip of polar boss. On the polar boss, strains decrease due to the effect of metal insert. The variations of hoop strains are small at the dome but near the tip of polar boss, hoop strains increase due to the increment of winding angle. On the polar boss, hoop strains are negligible due to the effect of metal insert. At the cylinder part, hoop strains increase due to the hoop stress

increment. In Fig. 13, the experimental results performed by Iida [21] can be shown. Finite element results are in reasonable agreement with the experimental results.

The fiber stress distributions the inner and outer ply are plotted along the length of the structure in Fig. 14a at the pressure  $P = 4.31 \text{ MPa}$ . The stresses in these figures do not mean the 2-P.K stresses but the Cauchy stresses. The fiber stress  $\sigma_{LL}$  in the angle ply is relatively constant at the dome part because of the isotensoid dome contour. But in the dome-cylinder junction area of the polar region, the fiber stresses in angle ply are maximum. In the hoop ply, the fiber stress at the cylinder part are maximum. These fiber stresses on the dome and cylinder parts are less than the unidirectional fiber strength which has the value of  $X = 1870 \text{ MPa}$ . The transverse fiber stress distribution is plotted in Fig 14b. The transverse fiber stress of angle ply is maximum at the tip of the polar boss because of the increment of the winding angle; the transverse fiber stress of the hoop ply is maximum at the cylinder part. The maximum value of it is  $49 \text{ MPa}$  which is close to the value of the transverse fiber strength of  $Y = 59.3 \text{ MPa}$ , so that the first ply failure may occur at the next load step. Considering the shear stress distribution in Fig 14c, The maximum value of it is  $29 \text{ MPa}$  which is much less than the shear strength of  $S = 99.6 \text{ MPa}$ . At that value of  $29 \text{ MPa}$ , the shear stress-shear strain relation is linear as shown in Fig. 4, so that when the only geometrical nonlinear analysis is compared with the geometrically and materially nonlinear analysis, the difference between them is negligible. By way of illustration, typical strain gage - load histories are depicted in Fig. 15 for the meridional and hoop strains at the location B at the Fig. 10. Just as finite element results shows linear behavior when the geometrical and material nonlinear analysis is performed, as the experimental results can be seen linear.

## CONCLUSIONS

An incremental Total Lagrangian Formulation is used for the degenerated composite shell elements that includes the effect of large rotation increments and material nonlinearity. The advantages of the new formulation over the standard formulation are to remove the restriction of small nodal rotations between two successive load increments and to permit large deformation and large rotations with good convergence. The results of the numerical tests demonstrate that the present model is suitable for

solving problems involving large rotations.

The results obtained from the analysis of a filament wound cylinder with angle-ply prove the efficiency of the present formulation in the material nonlinear analysis.

As a practical example, the filament wound pressure vessel is analyzed with the geometrically and materially nonlinearity taken into account. The numerical results agree well with the existing experimental results. For the case of CFRP pressure chamber, the effects of the materially nonlinearities are negligible due to the low shear stress level.

#### REFERENCES

1. A. K. Noor and S. J. Hartley, 'Nonlinear shell analysis via mixed isoparametric elements', *J. Computers & Structures*, **7**, 615-626 (1977).
2. S. Saigal, R. Kapania and T.Y. Yang, 'Geometrically Nonlinear Finite Element Analysis of Imperfect Laminated Shells', *J. Composite Material*, **20**, 197-214 (1986).
3. S. M. Jun and C. S. Hong, 'Buckling Behavior of Laminated Composite Cylindrical Panels under Axial Compression', *J. Computers & Structures*, **29**, 479-490 (1988).
4. J. H. Kweon and C. S. Hong, 'Postbuckling Analysis of Composite Laminated Cylindrical Panels Under Axial Compression', *AIAA J*, **31** (8), 1535-1537 (1993).
5. T. Y. Chang and K. Sawamiphakdi, 'Large Deformation Analysis of Laminated Shells By Finite Element Method', *J. Computers & Structures*, **13**, 331-340 (1981).
6. Y. H. Kim and S. W. Lee, 'A Solid Element Formulation For Large Deflection Analysis of Composite Shell Structures', *J. Computers & Structures*, **30**, 269-274 (1988).
7. K. S. Surana, 'Geometrically nonlinear formulation for the curved shell element', *Int. J. Num. Meth. Engng.*, **19**, 581-615 (1983).
8. J. C. Simo and L. Vu-Quoc, 'a Three-Dimensional Finite Strain Rod Model, Part II: Computational Aspects', *Computer Methods in Applied Mechanics and Engineering*, **58**, 79-116 (1986).
9. E. N. Dvorkin, Javier Oliver 'On a Non-Linear Formulation for Curved Timoshenko Beam Elements Considering Large Displacement/Rotation Increments', *Int. J. Num. Meth. Engin.*, **26**, 1597-1613 (1988).
10. J. Argyris, 'An excursion into large rotations', *Computer Methods in Applied Mechanics and Engineering*, **32**, 85-155 (1982).
11. H. T. Hahn and S. W. Tsai, 'Nonlinear Elastic Behavior of Unidirectional Composite Laminate', *J. Composite Mater*, **7**, 102-110 (1973).
12. H. Hu, 'Influence of Inplane Shear Nonlinearity on Buckling and Postbuckling Responses of Composite Plates and Shells', *J. Composite Mater*, **27**, 138-151 (1993).
13. M. Uemura and H. Fukunaga, 'Probabilistic Burst Strength of Filament-Wound Cylinders Under Internal Pressure', *J. Composit Mater*, **15**, 462-479 (1981).
14. L. Lemoine, 'Effects of Geometrical and Material Nonlinearities on Deflections of Filament-Wound Motor Chambers', *AIAA 78-1565* (1978).
15. J. P. Jeusette, G. Laschet, P. Chapentier and Ph. Deloo, 'Finite Element Analysis of Composite Revolution Structures Wound by Wide Plies', *Composite Structures*, **8**, 221-237 (1987).
16. M. Uemura, H. Iyama, H. Fukunaga, Y. Ikuta, and M. Morita, 'Developmental Research on Carbon Fiber Reinforced Plastic Rocket Motor Case', Rep. of Inst. Space and Aero. Sci., Univ. of Tokyo, **15**, No. 4, pp. 321 (1979).
17. H. Iida and M. Uemura, 'Mechanical Characteristics of Filament-Wound Pressure Vessel (Burst Pressure)', *Journal of Society of Space and Aeronautics Science of Japan*, **33**, 32-40 (1985).
18. T. J. R. Hughes, 'The FINITE ELEMENT METHOD', Prentice-Hall International, Inc., pp. 384-385, 1987.
19. E. Hinton and D. R. J. Owen, *Finite Element Software for Plates and Shells*, Pineridge Press, pp. 260-264, 1984.
20. K. J. Bathe, *Finite Element Procedures in Engineering Analysis*, Prentice Hall, Englewood Cliffs, New Jersey, 1982.
21. H. Iida and M. Uemura, 'Mechanical Characteristics of Filament-Wound Pressure Vessel (Burst Pressure)', *Journal of Society of Space and Aeronautics Science of Japan*, **33**, 32-40 (1985).
22. K. Y. Chang, S. Liu and F. K. Chang, 'Damage Tolerance of Laminated Composites Containing an Open Hole and Subjected to Tensile Loadings', *J. Composite Mater*, **25**, 274-301 (1991).

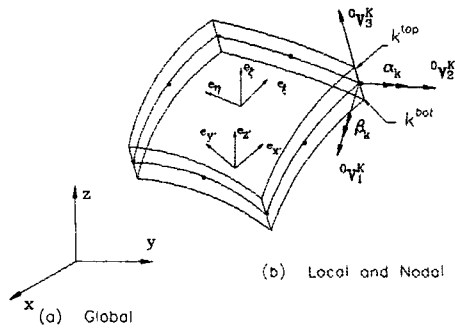


Fig. 1. Coordinate systems in degenerated shell formulation

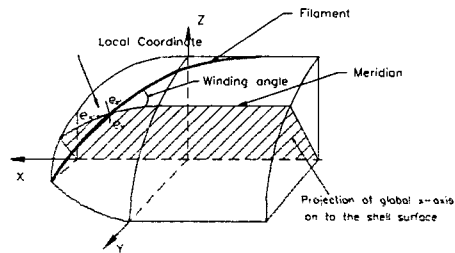


Fig. 2. Projection of global x-axis on to the shell surface

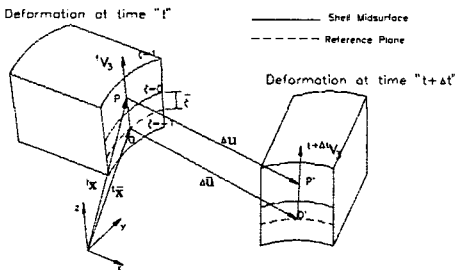


Fig. 3. Kinematics of shell deformation

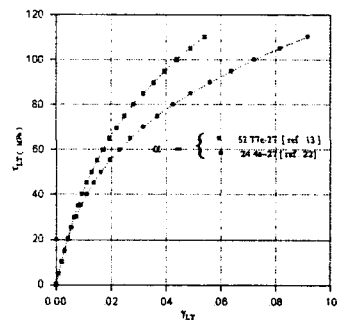


Fig. 4. Basic shear stress-shear strain relation of unidirectional graphite/epoxy

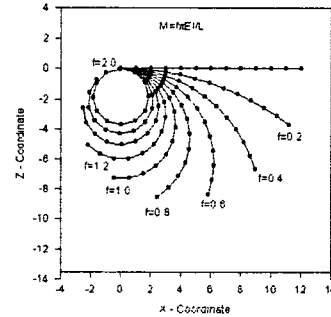


Fig. 5. Deformed shapes of the cantilever beam

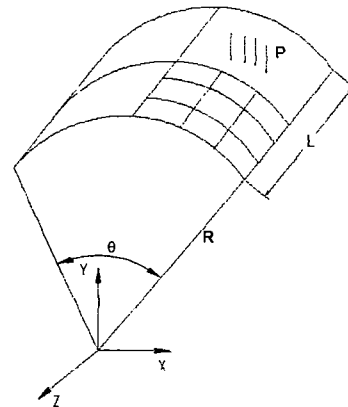


Fig. 6. Geometry, load versus deflection for clamped cross-ply cylinder shell under uniform load

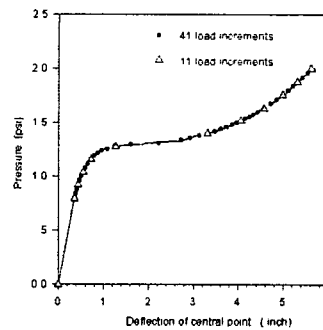


Fig. 7. Geometry, load versus central deflection for large deflection of clamped plate under uniform transverse loading

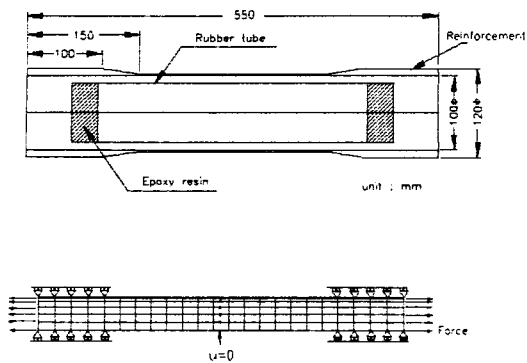


Fig. 8. Geometry of the GFRP helical wound cylinder and finite element model

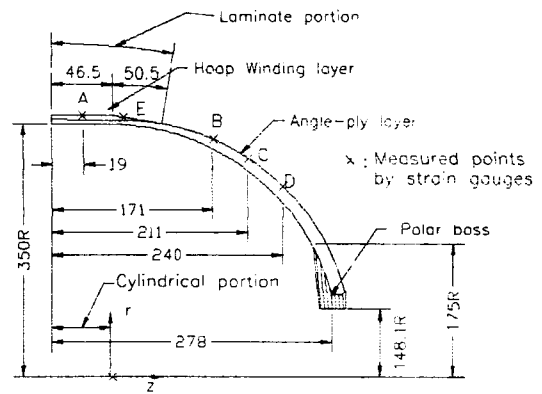


Fig. 10. Geometry of filament wound pressure chamber

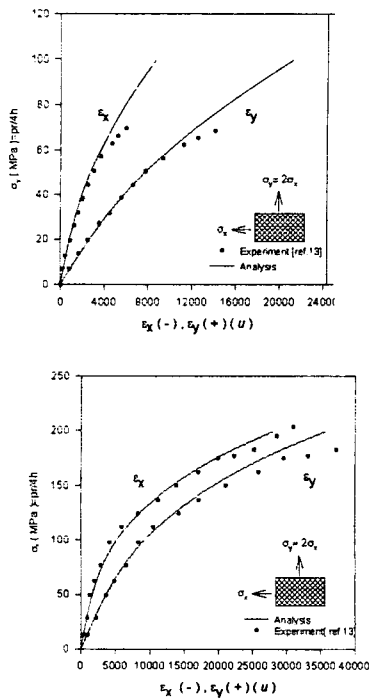


Fig. 9. Comparison of pressure-strains curves between F.E.M. results and experimental results :  $[\pm 35^\circ]_{8T}$  and  $[\pm 45^\circ]_{8T}$

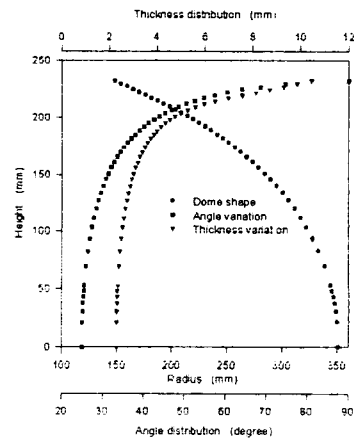


Fig. 11. Geodesic dome shape, angle variation, and thickness variation

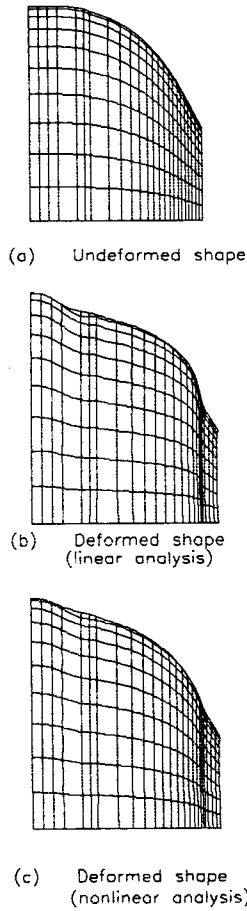


Fig. 12. Undeformed shape , deformed shape of linear analysis, and deformed shape of nonlinear analysis ( scaled displacement factor : 20)

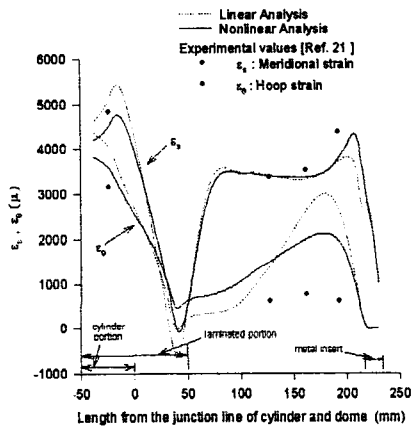


Fig. 13. Predicted and measured hoop and meridional strain (P=4.31 MPa)

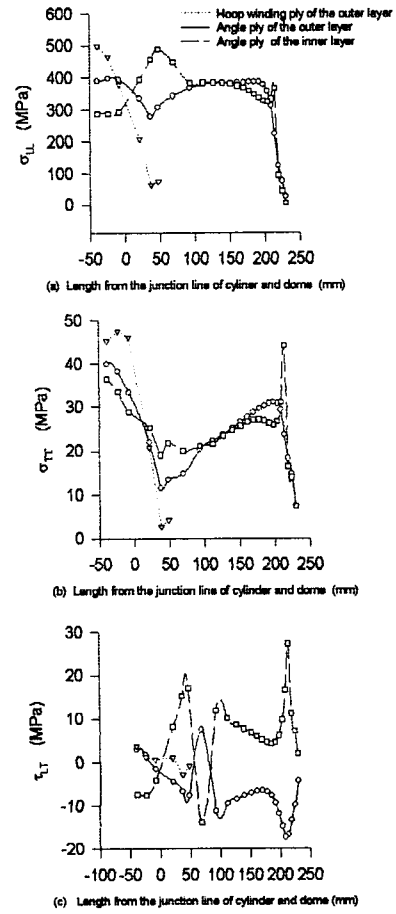


Fig. 14. Stress distribution of the outer layer and inner layer (P=4.31 MPa)

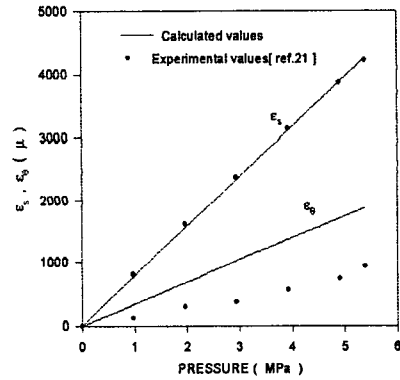


Fig. 15. Response of hoop and meridional strains at the location B